https://doi.org/10.1016/j.soildyn.2021.106753

Seismic performance of bridges with ECC-reinforced piers

Ning Zhang [a],·Quan Gu [a], You Dong [b], Jing Qian [b], Yue Zheng [c,*]

[a] *School of Architecture and Civil Engineering, Xiamen University, Xiamen, 361005, Fujian, P.R. China*

[b] *Department of Civil and Environmental Engineering, The Hong Kong Polytechnic University, Hong Kong, P.R. China*

[c] *Department of Bridge Engineering, Tongji University, Shanghai, 200092, P.R. China*

ABSTRACT Engineered cementitious composite (ECC) material, which is characterized by satisfactory resilience, moderate energy dissipation capacity as well as superhigh compressive and tensile strengths, has been widely applied to civil infrastructures (e.g., bridges, buildings, and coastal structures). To identify sensitive parameters, enhance resilience, and reduce cost of the ECC-reinforced structures effectively, a sensitivity analysis framework for the ECC-reinforced structures is necessary. In this regard, a uniaxial material model for the ECC material is firstly introduced and implemented in an open system for earthquake engineering simulation platform (OpenSees). A sensitivity analysis approach for the ECC material is proposed by deriving a series of sensitivity analysis equations at structure, element, and material levels based on direct differentiation method (DDM). The sensitivity analysis approach is integrated into the OpenSees and could be used directly for the ECC-reinforced structures. At last, the proposed ECC constitutive model are validated by three benchmark examples. The performance assessment and sensitivity analysis are conducted on a prototype bridge. The analyses results indicate that: (1) the earthquake-resistant and damage-control capacities of the ECC material are better than those of the normal concrete; (2) the DDM-based sensitivity analysis method is more efficient and accurate than the FDM-based one.

Keywords Finite element analysis; Sensitivity analysis; ECC material, Constitutive model; OpenSees.

---

* Corresponding author. Department of Bridge Engineering, Tongji University, Shanghai, 200092, P.R. China

E-mail address: yzheng@tongji.edu.cn (Y. Zheng).

1. Introduction

Reinforced concrete (RC) structures are vulnerable to severe damage or even collapse when they are subjected to disastrous earthquake events [1-3]. To improve the resilience of such damage-susceptible RC structures in earthquake-prone regions, a promising engineered cementitious composite (ECC) material, as a unique alternative to the conventional concrete material, is recommended for its inherent properties such as high tensile and compressive strengths, superior ductility, and moderate energy absorption capacity [4-7]. The ultimate tensile strain of the ECC material is usually up to 3% ~ 7%. The ECC material has satisfactory performance in safety, durability, applicability, etc., which can well compensate for various defects caused by brittleness and weak tensile properties of the traditional concrete material. It is demonstrated that the satisfactory resilience capacity endowed in the ECC material can effectively enhance the structural durability and functionality for bridges [8-12]. The ECC material is also used to reduce the permanently residual deformation of bridges for its excellent crack-controlling and energy-absorbing capacities [13, 14]. To further investigate the performance of ECC material and implement it in real practice, it is of paramount importance to develop the constitutive model. Several constitutive models for the ECC material have been developed in pioneering studies so far. For instance, Simo et al. [15] developed a constitutive model based on the thermodynamics and damage-mechanics theories, which can be used to simulate crack propagation of the ECC material. Borst and Nauta [16] proposed a multiple fixed cracking model for non-orthogonal crack description in a continuum formulation. The aforementioned two constitutive models are complex and time consuming when conducting numerical simulation, which is only suitable for small scale model. Han et al. [17, 18] developed a uniaxial constitutive model that can be utilized to accurately simulate strain hardening and stable hysteresis performance of the ECC material. This constitutive model was employed to solve two-dimension problems.

In addition, the variability effect of the key parameters controlling the hysteretic model on the seismic performance of the ECC-reinforced structures has not been investigated comprehensively. This effect could be revealed by sensitivity analysis. Sensitivity analysis aims to identify the critical parameters of the system to the response and is an essential procedure prior to optimizing the ECC-reinforced structures. More attention should be paid on the identified sensitive parameters during design or optimization process. There are several approaches to accomplish the sensitivity analysis, such as finite difference method (FDM), perturbation method (PM), adjoint method (AM), and direct differentiation method (DDM).

These methods have been systematically studied so far [19-25]. FDM is a kind of numerical solution which transforms the problem of solving differential equation into solving difference equation in mechanics. It is the simplest method among them for response sensitivity computation but is time-consuming. Another drawback is that it is vulnerable to be contaminated by numerical noise [26, 27]. The AM is unsuitable for such problems that are related to historical paths. The accuracy from the PM is the lowest among the three methods. Therefore, the DDM is recommended to conduct sensitivity analysis for its high accuracy and computational efficiency. Moreover, it can be easily applied to any material constitutive models (e.g., history-dependent models such as ECC material) and is suitable for complicated structural systems [28, 29]. Although many researchers have extended the sensitivity analysis to normal concrete material in the past two decades [30-32], the DDM-based sensitivity analysis for the ECC material has not been established so far. Also, there is a lack of an efficient and practical tool to analyze the sensitivity for the ECC-reinforced component and structure. In this regard, the DDM-based sensitivity analysis approach is firstly derived and then it is integrated into an open system for earthquake engineering simulation platform (OpenSees) [33]. In this way, the gap between the DDM-based sensitivity analysis and the FE method is filled. After performing sensitivity analysis, the sensitive and insensitive parameters could be determined. The insensitive parameters may be neglected in optimization process, while the identified sensitive parameters could be regarded as primary design or optimization variables.

In summary, a DDM-based sensitivity analysis framework for the ECC-reinforced structures is developed and implemented in OpenSees. A simplified and efficient uniaxial constitutive model for the ECC material is firstly introduced and implemented into the OpenSees. The DDM-based dynamic equilibrium equations by virtue of Newmark-β method for the sensitivity analysis at structure level are subsequently derived. This theoretical work is further extended to the element and material levels. Thus, a systematical sensitivity analysis algorithm is developed. The sensitivity analysis algorithm is integrated into OpenSees for the ECC-reinforced structures. To illustrate the developed framework, application examples are conducted. Two FE models of a prototype bridge located in earthquake-prone are established in OpenSees, respectively, of which only the materials of the columns are different (i.e., one is conventional RC pier and another is ECC-reinforced pier). The seismic performance of the two bridges under earthquake loads is compared. Both the DDM- and FDM-based sensitivity analysis frameworks are applied to the ECC-reinforced bridge for comparison in terms of computational accuracy and efficiency. A series of sensitivity analysis studies on the ECC-reinforced and RC bridges under earthquake loads are carried out. Based on the results of this

study, it can be concluded that the sensitivity ranking of the material parameters associated with the ECC material, normal concrete, and reinforcing steel used in the two bridges may vary with time.

2. Constitutive model of ECC material and validation

The ECC material is an innovative ultra-ductile fiber reinforced concrete that has metal-like features especially when it sustains tensile loads. The distinguish metal-like material mainly consists of cement, sand (maximum particle size 0.3 mm), superplasticizer, water, common admixtures and 1.5% polyethylene fiber in volume [34].

To analysis ECC-reinforced structures under dynamic loads (e.g., earthquake loads), a constitutive model is essential. Therefore, a uniaxial constitutive model for the ECC material proposed by Han et al. [17], named *ECC02*, is employed and integrated into OpenSees. The envelop curves of the uniaxial constitutive model for the ECC material are illustrated in Fig. 1. The envelop curve in tension is multilinear curves consisting of four segments which are expressed as Eq. 1, and the envelop curve in compression is also multilinear curves composed of three segments which are written as Eq. 2.

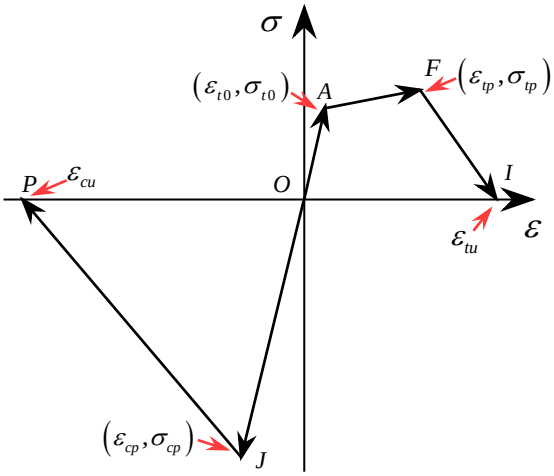

Fig. 1. Envelop curves of the ECC constitutive model

There is a strain hardening stage (i.e., segment *A*-*F*) in the tension region, which demonstrates that the ECC material has better resilient capacity than the normal concrete. The three segments on the envelope curve within the tensile region (i.e., segments *O*-*A*-*F*-*I*) are expressed as

$$F_t = \begin{cases} E\varepsilon & 0 \le \varepsilon \le \varepsilon_{t0} \\ \sigma_{t0} + \left(\sigma_{tp} - \sigma_{t0}\right)\dfrac{\left(\varepsilon - \varepsilon_{t0}\right)}{\left(\varepsilon_{tp} - \varepsilon_{t0}\right)} & \varepsilon_{t0} \le \varepsilon < \varepsilon_{tp} \\ \sigma_{tp}\dfrac{\left(\varepsilon_{tu} - \varepsilon\right)}{\left(\varepsilon_{tu} - \varepsilon_{tp}\right)} & \varepsilon_{tp} \le \varepsilon < \varepsilon_{tu} \\ 0 & \varepsilon_{tu} \le \varepsilon \end{cases} \tag{1}$$

where E is Young's modulus. The first microcrack will occur once the strain ε is larger than the cracking strain ε_{t0} (i.e., point A). The continuously loading path then follows the segment A-F until the strain reaches the peak tensile strain ε_{tp} at point F, where the stress simultaneously reaches the peak tensile stress σ_{tp}. However, a soft stiffness (i.e., segment F-I) will emerge if the tensile strain exceeds ε_{tp} but is smaller than the ultimate tensile strain ε_{tu} at point I, where the corresponding stress becomes zero. It is worth noting that the loading path will continuously move forward along the positive abscissa axis if the strain is larger than ε_{tu}.

The envelope curve is represented as multilinear curves in the compressive region (i.e., segments O-J-P) which can be written as

$$F_c = \begin{cases} E\varepsilon & \varepsilon_{tp} \le \varepsilon < 0 \\ \sigma_{cp}\dfrac{\left(\varepsilon_{cu} - \varepsilon\right)}{\left(\varepsilon_{cu} - \varepsilon_{cp}\right)} & \varepsilon_{cp} \le \varepsilon < \varepsilon_{cu} \\ 0 & \varepsilon_{cu} \le \varepsilon \end{cases} \tag{2}$$

where σ_{cp} and ε_{cp} are the peak compressive stress and corresponding strain, respectively. ε_{cu} represents the ultimate compressive strain. It is noted that loading path will further move forward along the negative abscissa axis if the strain is smaller than ε_{cu}.

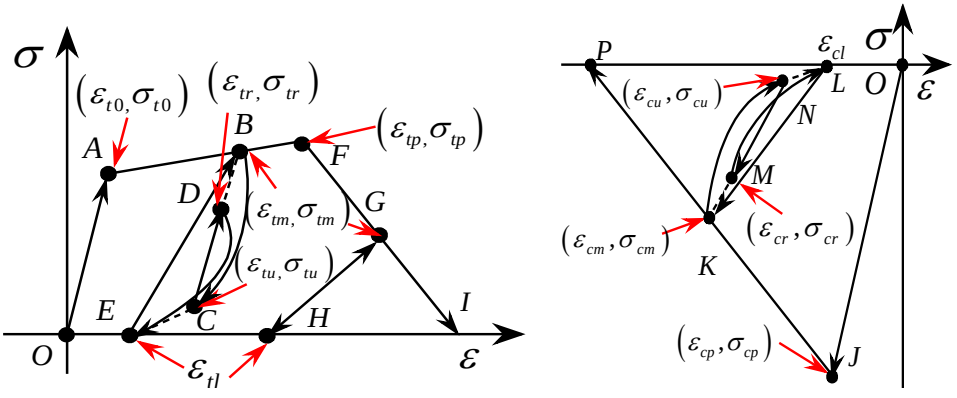

(a) (b)

Fig. 2. Unloading and reloading of the ECC model (a) Tension region and (b) Compression region

The loading as well as the unloading and reloading rules of the ECC model in the tension region (see Fig. 2a) are formulated as

$$F_t = \begin{cases} E\varepsilon & 0 \le \varepsilon_{tm} < \varepsilon_{t0} \quad (3a) \\ \sigma_{tl}^{'}\left(\dfrac{\varepsilon-\varepsilon_{tl}}{\varepsilon_{tm}^{'}-\varepsilon_{tl}}\right)^{\alpha_t} & \varepsilon_{t0} \le \varepsilon_{tm} < \varepsilon_{tp}, \dot{\varepsilon} < 0 \quad (3b) \\ \sigma_{tl}^{'} + \left(\sigma_{tm}-\sigma_{tl}^{'}\right)\left(\dfrac{\varepsilon-\varepsilon_{tl}^{'}}{\varepsilon_{tm}^{'}-\varepsilon_{tl}^{'}}\right) & \varepsilon_{t0} \le \varepsilon_{tm} < \varepsilon_{tp}, \dot{\varepsilon} \ge 0 \quad (3c) \\ \sigma_{tm}\left(\dfrac{\varepsilon-\varepsilon_{tl}}{\varepsilon_{tm}-\varepsilon_{tl}}\right) & \varepsilon_{tp} \le \varepsilon_{tm} < \varepsilon_{tu} \quad (3d) \end{cases}$$

where α_t is a constant material parameter that is larger than or equal to 1. It can be calibrated according to the experimental data. The segment *B*-*C*-*E* is called initial unloading path expressed by the Eq. 3b. ε_{tm} presents the historically reached maximum strain on the envelop curve where the unloading is triggered. ε_{tl} is the strain corresponding to the stress vanishing on the initial unloading path (i.e., the strain associated with the point *E* or *H*). The value $\varepsilon_{tl} = \beta_t \cdot \varepsilon_{tm}$, where β_t is a constant. The segment *C*-*D* is a typically partial reloading path (since the stress at point *C* is not zero) expressed by Eq. 3c, which guarantees the extension of the segment *C*-*D* passing through the historically reached maximum strain point on the envelop curve (i.e., point *B*). The ε_{tr} and ε_{tu} are strains at points *C* and *D*, respectively. The unloading path starting from *D* is dominated by Eq. 3b. The subscript on the parameter $\varepsilon_{tm}^{'}$ denotes that $\varepsilon_{tm}^{'}$ should be set as ε_{tm} or ε_{tr} when they are used to define the initial unloading path or partially reloading path, respectively. The same specification applies to the parameters $\varepsilon_{tl}^{'}$ and $\varepsilon_{tu}^{'}$. The unloading and reloading paths after point *F* (i.e., *F*-*G*) are a linear curve expressed by Eq. 3d. The loading as well as the unloading and reloading paths of the ECC model in the compression region (see Fig. 2b) can be given as

$$F_c = \begin{cases} E\varepsilon & \varepsilon_{cp} \le \varepsilon_{cm} < 0 \quad (4a) \\ \sigma_{cm}^{'}\left(\dfrac{\varepsilon-\varepsilon_{cl}}{\varepsilon_{cm}^{'}-\varepsilon_{cl}}\right)^{\alpha_c} & \varepsilon_{cu} \le \varepsilon_{cm} < \varepsilon_{cp}, \dot{\varepsilon} > 0 \quad (4b) \\ \sigma_{cu}^{'} + \left(\sigma_{cm}-\sigma_{cm}^{'}\right)\left(\dfrac{\varepsilon-\varepsilon_{cl}^{'}}{\varepsilon_{cm}^{'}-\varepsilon_{cl}^{'}}\right) & \varepsilon_{cu} \le \varepsilon_{cm} < \varepsilon_{cp}, \dot{\varepsilon} \le 0 \quad (4c) \end{cases}$$

As shown in Fig. 2b, the segment *K*-*N* is formulated by Eq. 4b. The ε_{cm} is the strain on the envelope curve where unloading is triggered (i.e., the strain at point *K*) and the ε_{cl} is the strain on the initial unloading path corresponding to zero stress (i.e., the strain at point *L*). The value $\varepsilon_{cl} = \beta_c \cdot \varepsilon_{cm}$, where β_c is a constant. The segment *N*-*M* is expressed by Eq. 4c. The ε_{cr} and ε_{cu} are strains of the points *M* and *N*, respectively. The unloading path from *N* is dominated by Eq. 4b. The parameter $\varepsilon_{cm}^{'}$ should be set to ε_{cm} or ε_{cr} when they are used to define the initial unloading path or partially reloading path.

3. Sensitivity analysis

The response sensitivity to material parameter is defined as $\frac{\partial \mathbf{R}}{\partial \theta}$, where $\mathbf{R}$ represents the structural response and θ denotes the investigated material parameter. For the ECC material, a total of 12 critical material parameters are considered for sensitivity analysis, including five parameters governing the tensile state (i.e., σ_{t0}, ε_{t0}, σ_{tp}, ε_{tp} and ε_{tu}), three parameters controlling the compressive state (i.e., σ_{c0}, ε_{c0} and ε_{cp}) and four parameters related to the hysteretic performance (i.e., α_t, α_c, β_t, and β_c). The DDM-based response sensitivity analysis requires differentiating the response against the parameter θ at structure, element and material levels, respectively.

3.1. DDM-based sensitivity analysis at structural and element levels

In order to conveniently interpret how to conduct the sensitivity analysis of a structure subjected to earthquake loads, a numerical calculation method is necessary. The well-known Newmark-β method is selected to solve the structural dynamic equations in this study. Thus, the discretized equation of the response sensitivity at each analysis time step can be expressed as

$$\begin{aligned}&\left[\frac{1}{\beta(\Delta t)^2}\mathbf{M} + \frac{\alpha}{\beta(\Delta t)}\mathbf{C} + (\mathbf{K})_{n+1}\right]\frac{\partial \mathbf{u}_{n+1}}{\partial \theta} \\ &= -\left(\frac{1}{\beta(\Delta t)^2}\frac{d\mathbf{M}}{d\theta} + \frac{\alpha}{\beta(\Delta t)}\frac{d\mathbf{C}}{d\theta}\right)\mathbf{u}_{n+1} - \left.\frac{\partial \mathbf{R}(\mathbf{u}_{n+1}(\theta),\theta)}{\partial \theta}\right|_{\mathbf{u}_{n+1}} + \frac{\partial \tilde{\mathbf{F}}_{n+1}}{\partial \theta}\end{aligned} \tag{5}$$

where,

$$\begin{aligned}\frac{\partial \tilde{\mathbf{F}}_{n+1}}{\partial\theta}=&\frac{\partial \mathbf{F}_{n+1}}{\partial\theta}+\frac{\partial \mathbf{M}}{\partial\theta}\left(\frac{1}{\beta(\Delta t)^2}\mathbf{u}_n+\frac{1}{\beta(\Delta t)}\dot{\mathbf{u}}_n-\left(1-\frac{1}{2\beta}\right)\ddot{\mathbf{u}}_n\right)\\&+\mathbf{M}\left[\frac{1}{\beta(\Delta t)^2}\frac{\partial \mathbf{u}_n}{\partial\theta}+\frac{1}{\beta(\Delta t)}\frac{\partial \dot{\mathbf{u}}_n}{\partial\theta}-\left(1-\frac{1}{2\beta}\right)\frac{\partial \ddot{\mathbf{u}}_n}{\partial\theta}\right]\\&+\frac{\partial \mathbf{C}}{\partial\theta}\left(\frac{\alpha}{\beta(\Delta t)}\mathbf{u}_n-\left(1-\frac{\alpha}{\beta}\right)\dot{\mathbf{u}}_n-\Delta t\left(1-\frac{\alpha}{2\beta}\right)\ddot{\mathbf{u}}_n\right)\\&+\mathbf{C}\left[\frac{\alpha}{\beta(\Delta t)}\frac{\partial \mathbf{u}_n}{\partial\theta}-\left(1-\frac{\alpha}{\beta}\right)\frac{\partial \dot{\mathbf{u}}_n}{\partial\theta}-\Delta t\left(1-\frac{\alpha}{2\beta}\right)\frac{\partial \ddot{\mathbf{u}}_n}{\partial\theta}\right]\end{aligned}\tag{6}$$

M and **C** represent the mass and damping matrices of the investigated structure, respectively. α and β are constant parameters. **K** represents the tangent stiffness matrix of the structure. Δt represents the time increment. $\tilde{\mathbf{F}}$ represents the predicted response of the structure in the elastic state, which can be calculated by Eq. 6. **F** is the external force vector. $\mathbf{u}$, $\dot{\mathbf{u}}$, and $\ddot{\mathbf{u}}$ represent the displacement, velocity and acceleration, respectively. θ represents the material parameters. In Eq. 5, a crucial term at the right-hand side is $\left.\frac{\partial \mathbf{R}(\mathbf{u}_{n+1}(\theta),\theta)}{\partial\theta}\right|_{\mathbf{u}_{n+1}}$ which indicates the partial derivation of the internal resisting force $\mathbf{R}(\mathbf{u}_{n+1})$ against the material parameter θ. The $|_{\mathbf{u}_{n+1}}$ indicates that the variable is evaluated under the condition that the displacement $\mathbf{u}_{n+1}$ remains fixed. The conditional internal resisting force sensitivity can be obtained by assembling the contributions from all elements

$$\left.\frac{\partial \mathbf{R}(\mathbf{u}_{n+1})}{\partial\theta}\right|_{\mathbf{u}_{n+1}}=\mathop{\mathbf{A}}_{e=1}^{nel}\left(\int_{\Omega^e}\mathbf{B}^{\mathrm{T}}(\mathbf{x})\left.\frac{\partial \boldsymbol{\sigma}(\boldsymbol{\varepsilon}_{n+1}(\theta),\theta)}{\partial\theta}\right|_{\boldsymbol{\varepsilon}_{n+1}}d\Omega^e\right)\tag{7}$$

where $\mathop{\mathbf{A}}_{n=1}^{nel}(\ )$ denotes the stiffness assembly operator. *nel* represents the number of elements in the FE model, and $\mathbf{B}$ is the strain-displacement transformation matrix. From Eq. 7, it can be observed that the stress sensitivities under fixed displacement $\left.\frac{\partial \boldsymbol{\sigma}(\boldsymbol{\varepsilon}_{n+1}(\theta),\theta)}{\partial\theta}\right|_{\boldsymbol{\varepsilon}_{n+1}}$ at material level should be achieved before solving the unknown displacement sensitivity $\frac{\mathrm{d}\mathbf{u}_{n+1}}{\mathrm{d}\theta}$. The conditional stress sensitivity is a special case of the unconditional one and can be calculated by simply setting $\frac{\partial \boldsymbol{\varepsilon}_{n+1}}{\partial\theta}=0$. The calculation method of the unconditional stress sensitivity $\frac{\partial \boldsymbol{\sigma}(\boldsymbol{\varepsilon}_{n+1}(\theta),\theta)}{\partial\theta}$ at material level will be addressed in the following section.

3.2. DDM-based sensitivity analysis at material level

As mentioned earlier, the DDM-based response sensitivity analysis at the material level can be successfully achieved only after the stress calculation process finishes at each time-step. Both the conditional and the unconditional stress sensitivity analysis procedures include two parts: one part is associated with the envelop curves and the other part is related to the unloading and reloading schemes.

For the unconditional case, the stress sensitivity of the envelope curve (i.e., part one) in the tensile region can be calculated by differentiating Eq. 1 against the parameter θ, which can be expressed as

$$\frac{\partial \sigma}{\partial \theta}=\begin{cases}\dfrac{\partial E}{\partial \theta}\varepsilon+E\dfrac{\partial \varepsilon}{\partial \theta} & 0\le \varepsilon<\varepsilon_{t0}\\ \dfrac{\partial \sigma_{t0}}{\partial \theta}+\left(\dfrac{\partial \sigma_{tp}}{\partial \theta}-\dfrac{\partial \sigma_{t0}}{\partial \theta}\right)\left(\dfrac{\varepsilon-\varepsilon_{t0}}{\varepsilon_{tp}-\varepsilon_{t0}}\right) & \\ +\left(\sigma_{tp}-\sigma_{t0}\right)\left(\dfrac{\partial \varepsilon}{\partial \theta}\dfrac{1}{\left(\varepsilon_{tp}-\varepsilon_{t0}\right)}+\dfrac{\partial \varepsilon_{t0}}{\partial \theta}\dfrac{\left(\varepsilon-\varepsilon_{tp}\right)}{\left(\varepsilon_{tp}-\varepsilon_{t0}\right)^2}+\dfrac{\partial \varepsilon_{tp}}{\partial \theta}\dfrac{\left(\varepsilon_{t0}-\varepsilon\right)}{\left(\varepsilon_{tp}-\varepsilon_{t0}\right)^2}\right) & \varepsilon_{t0}\le \varepsilon<\varepsilon_{tp}\\ \dfrac{\partial \sigma_{tp}}{\partial \theta}\left(\dfrac{\varepsilon_{tu}-\varepsilon}{\varepsilon_{tu}-\varepsilon_{tp}}\right)-\sigma_{tp}\left(\dfrac{\partial \varepsilon}{\partial \theta}\dfrac{1}{\left(\varepsilon_{tu}-\varepsilon_{tp}\right)}+\dfrac{\partial \varepsilon_{tp}}{\partial \theta}\dfrac{\left(\varepsilon-\varepsilon_{tu}\right)}{\left(\varepsilon_{tu}-\varepsilon_{tp}\right)^2}+\dfrac{\partial \varepsilon_{tu}}{\partial \theta}\dfrac{\left(\varepsilon_{tp}-\varepsilon\right)}{\left(\varepsilon_{tu}-\varepsilon_{tp}\right)^2}\right) & \varepsilon_{tp}\le \varepsilon<\varepsilon_{tu}\end{cases} \tag{8}$$

Similarly, the stress sensitivities of the envelop curve in the compression region (i.e., part one) can be derived from Eq. 2 and written as

$$\frac{\partial \sigma}{\partial \theta}=\begin{cases}\dfrac{\partial E}{\partial \theta}\varepsilon+E\dfrac{\partial \varepsilon}{\partial \theta} & \varepsilon_{cp}\le \varepsilon<0\\ \dfrac{\partial \sigma_{cp}}{\partial \theta}\left(\dfrac{\varepsilon_{cu}-\varepsilon}{\varepsilon_{cu}-\varepsilon_{cp}}\right)-\sigma_{cp}\left(\dfrac{\partial \varepsilon}{\partial \theta}\dfrac{1}{\left(\varepsilon_{cu}-\varepsilon_{cp}\right)}+\dfrac{\partial \varepsilon_{cp}}{\partial \theta}\dfrac{\left(\varepsilon-\varepsilon_{cu}\right)}{\left(\varepsilon_{cu}-\varepsilon_{cp}\right)^2}+\dfrac{\partial \varepsilon_{cu}}{\partial \theta}\dfrac{\left(\varepsilon_{cp}-\varepsilon\right)}{\left(\varepsilon_{cu}-\varepsilon_{cp}\right)^2}\right) & \varepsilon_{cp}\le \varepsilon<\varepsilon_{cu}\end{cases} \tag{9}$$

For the unloading and reloading rules, the stress sensitivities in the tension region (i.e., part two) can be derived from Eq. 3 and expressed as

$$\frac{\partial \sigma}{\partial \theta}=\begin{cases}\dfrac{\partial E}{\partial \theta}\varepsilon+E\dfrac{\partial \varepsilon}{\partial \theta} & 0\le \varepsilon_{tm}<\varepsilon_{t0}\\ \dfrac{\partial \sigma_{tm}^{'}}{\partial \theta}\left(\dfrac{\varepsilon-\varepsilon_{tl}}{\varepsilon_{tm}^{'}-\varepsilon_{tl}}\right)^{\alpha_t}+\sigma_{tm}^{'}\left(\dfrac{\varepsilon-\varepsilon_{tl}}{\varepsilon_{tm}^{'}-\varepsilon_{tl}}\right)^{\alpha_t}\left(\dfrac{\partial \alpha_t}{\partial \theta}\ln\left(\dfrac{\varepsilon-\varepsilon_{tl}}{\varepsilon_{tm}^{'}-\varepsilon_{tl}}\right)+\dfrac{\alpha_t}{\varepsilon-\varepsilon_{tl}}\left(\dfrac{\partial \varepsilon}{\partial \theta}-\dfrac{\partial \varepsilon_{tl}}{\partial \theta}-\dfrac{\left(\varepsilon-\varepsilon_{tl}\right)}{\left(\varepsilon_{tm}^{'}-\varepsilon_{tl}\right)}\left(\dfrac{\partial \varepsilon_{tm}^{'}}{\partial \theta}-\dfrac{\partial \varepsilon_{tl}}{\partial \theta}\right)\right)\right) & \varepsilon_{t0}\le \varepsilon_{tm}<\varepsilon_{tp},\dot{\varepsilon}<0\\ \dfrac{\partial \sigma_{tl}^{'}}{\partial \theta}+\left(\dfrac{\partial \sigma_{tm}}{\partial \theta}-\dfrac{\partial \sigma_{tl}^{'}}{\partial \theta}\right)\left(\dfrac{\varepsilon-\varepsilon_{tl}^{'}}{\varepsilon_{tm}^{'}-\varepsilon_{tl}^{'}}\right)+\left(\sigma_{tm}-\sigma_{tl}^{'}\right)\left(\dfrac{\partial \varepsilon}{\partial \theta}\dfrac{1}{\left(\varepsilon_{tm}^{'}-\varepsilon_{tl}^{'}\right)}+\dfrac{\partial \varepsilon_{tl}^{'}}{\partial \theta}\dfrac{\left(\varepsilon-\varepsilon_{tm}^{'}\right)}{\left(\varepsilon_{tm}^{'}-\varepsilon_{tl}^{'}\right)^2}+\dfrac{\partial \varepsilon_{tm}^{'}}{\partial \theta}\dfrac{\left(\varepsilon_{tl}^{'}-\varepsilon\right)}{\left(\varepsilon_{tm}^{'}-\varepsilon_{tl}^{'}\right)^2}\right) & \varepsilon_{t0}\le \varepsilon_{tm}<\varepsilon_{tp},\dot{\varepsilon}\ge 0\\ \dfrac{\partial \sigma_{tm}}{\partial \theta}\left(\dfrac{\varepsilon-\varepsilon_{tl}}{\varepsilon_{tm}-\varepsilon_{tl}}\right)+\sigma_{tm}\left(\dfrac{\partial \varepsilon}{\partial \theta}\dfrac{1}{\left(\varepsilon_{tm}-\varepsilon_{tl}\right)}+\dfrac{\partial \varepsilon_{tl}}{\partial \theta}\dfrac{\left(\varepsilon-\varepsilon_{tm}\right)}{\left(\varepsilon_{tm}-\varepsilon_{tl}\right)^2}+\dfrac{\partial \varepsilon_{tm}}{\partial \theta}\dfrac{\left(\varepsilon_{tl}-\varepsilon\right)}{\left(\varepsilon_{tm}-\varepsilon_{tl}\right)^2}\right) & \varepsilon_{tp}\le \varepsilon_{tm}<\varepsilon_{tu}\end{cases} \tag{10}$$

It should be noted that ε_{tl}, ε_{tm}, σ_{tl} and σ_{tm} are functions of the material parameters. The

stress sensitivities should be calculated and then saved at each time step for calling and updating during the computational process. Similarly, the stress sensitivities of the unloading and reloading schemes in the compressive region (i.e., part two) can be derived from Eq. 4 and written as

$$\frac{\partial \sigma}{\partial \theta}=\begin{cases}\dfrac{\partial E}{\partial \theta}\varepsilon+E\dfrac{\partial \varepsilon}{\partial \theta} & \varepsilon_{cp}\le\varepsilon_{cm}<0\\ \dfrac{\partial \sigma_{cm}^{'}}{\partial \theta}\left(\dfrac{\varepsilon-\varepsilon_{cl}}{\varepsilon_{cm}^{'}-\varepsilon_{cl}}\right)^{\alpha_c}+\sigma_{cm}^{'}\left(\dfrac{\varepsilon-\varepsilon_{cl}}{\varepsilon_{cm}^{'}-\varepsilon_{cl}}\right)^{\alpha_c}\left(\dfrac{\partial \alpha_c}{\partial \theta}\ln\left(\dfrac{\varepsilon-\varepsilon_{cl}}{\varepsilon_{cm}^{'}-\varepsilon_{cl}}\right)+\dfrac{\alpha_c}{\varepsilon-\varepsilon_{cl}}\left(\dfrac{\partial \varepsilon}{\partial \theta}-\dfrac{\partial \varepsilon_{cl}}{\partial \theta}-\dfrac{(\varepsilon-\varepsilon_{cl})}{(\varepsilon_{cm}^{'}-\varepsilon_{cl})}\left(\dfrac{\partial \varepsilon_{cm}^{'}}{\partial \theta}-\dfrac{\partial \varepsilon_{cl}}{\partial \theta}\right)\right)\right) & \varepsilon_{cu}\le\varepsilon_{cm}<\varepsilon_{cp},\dot{\varepsilon}>0\\ \dfrac{\partial \sigma_{cu}^{'}}{\partial \theta}+\left(\dfrac{\partial \sigma_{cm}}{\partial \theta}-\dfrac{\partial \sigma_{cm}^{'}}{\partial \theta}\right)\left(\dfrac{\varepsilon-\varepsilon_{cl}^{'}}{\varepsilon_{cm}^{'}-\varepsilon_{cl}^{'}}\right)+\left(\sigma_{cm}-\sigma_{cm}^{'}\right)\dfrac{\left(\dfrac{\partial \varepsilon}{\partial \theta}-\dfrac{\partial \varepsilon_{cl}^{'}}{\partial \theta}\right)\left(\varepsilon_{cm}^{'}-\varepsilon_{cl}^{'}\right)-\left(\varepsilon-\varepsilon_{cl}^{'}\right)\left(\dfrac{\partial \varepsilon_{cm}^{'}}{\partial \theta}-\dfrac{\partial \varepsilon_{cl}^{'}}{\partial \theta}\right)}{\left(\varepsilon_{cm}^{'}-\varepsilon_{cl}^{'}\right)^{2}} & \varepsilon_{cu}\le\varepsilon_{cm}<\varepsilon_{cp},\dot{\varepsilon}\le 0\end{cases} \tag{11}$$

To sum up, both the conditional and the unconditional response sensitivities can be evaluated only after the stress sensitivity is calculated at each time step. Firstly, the unconditional stress sensitivity can be obtained through Eqs. 8-11. Subsequently the $\left.\dfrac{\partial \mathbf{R}\left(\mathbf{u}_{n+1}(\theta),\theta\right)}{\partial \theta}\right|_{\mathbf{u}_{n+1}}$ is assembled using Eq. 7 and the response sensitivity is finally evaluated via Eq. 6. The strain sensitivity $\dfrac{\partial \varepsilon_{n+1}}{\partial \theta}$ can be solved from the formulation of the strain and displacement, i.e., $\dfrac{\partial \varepsilon_{n+1}}{\partial \theta}=\mathbf{B}\dfrac{\partial \mathbf{u}_{n+1}}{\partial \theta}$. The conditional sensitivities can also be obtained from the same equations Eqs. 8-11 and the supplementary condition of the fixed displacement/strain. Thus, the unconditional sensitivity analysis converts to the conditional one. It's worth noting that the seismic response of the ECC material is dependent on its historical paths, the sensitivities of such variables (e.g., $\dfrac{\partial \varepsilon_{tr}}{\partial \theta}$, $\dfrac{\partial \varepsilon_{tm}}{\partial \theta}$, $\dfrac{\partial \sigma_{tr}}{\partial \theta}$ and $\dfrac{\partial \sigma_{tm}}{\partial \theta}$) should be saved for repeatedly calling and updating in the following analysis steps.

4. Validation of ECC constitutive model

In order to demonstrate the applicability and accuracy of the ECC-reinforced constitutive model which has been implemented in OpenSees, three application examples (i.e., ECC-reinforced cantilever column under reversal cyclic loading, RC-ECC reinforced bridge pier under reversal cyclic loading and ECC-reinforced plane frame under earthquake ground motion) were numerically simulated, and the numerical results were validated by test ones.

4.1.1 ECC-reinforced cantilever column under reversal cyclic loading

The tested cantilever column used is 0.5 m high, square section, and the section size is 100 mm × 100 mm [17], as shown in Fig. 3. The longitudinal reinforcement was provided by four bars with a diameter of 10 mm and arranged symmetrically in four corners. The cross-section adopted the core area size of 80 mm × 80 mm with a cover layer thickness of 10 mm. A horizontal force was applied at the top of the column using a displacement-control loading protocol. The diagram of the column and the loading protocol are shown in Fig. 4, respectively. The maximum horizontal displacement was 75 mm and the peak drift ratio was up to 0.15. The nonlinear finite element (FE) model of the column was established in OpenSees. A total of five displacement-based Euler-Bernoulli fiber beam-column elements were used to model the ECC-reinforced column. The material nonlinearities of the ECC and reinforcement were considered using *ECC02* and *Steel02* materials, respectively. The designed parameters of the ECC material are presented in Table 1, where four parameters related to the hysteretic performance (i.e., α_t, α_c, β_t, and β_c) are taken as 5.0, 2.0, 0.4 and 0.3, respectively. The values of the parameters determine the energy consumption capacity of ECC, which needs to be calibrated by uniaxial tension/compression test. Additionally, the geometric nonlinearity of the column was considered using corotational transformation algorithm.

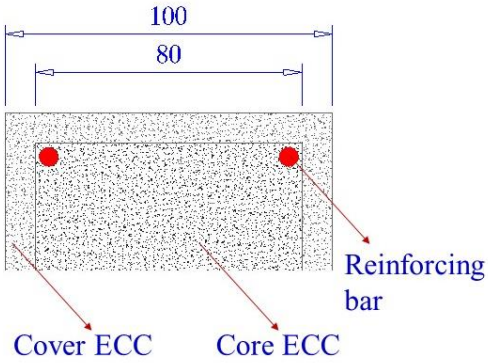

Fig. 3. Cross-Section of cantilever column diagram (unit: mm)

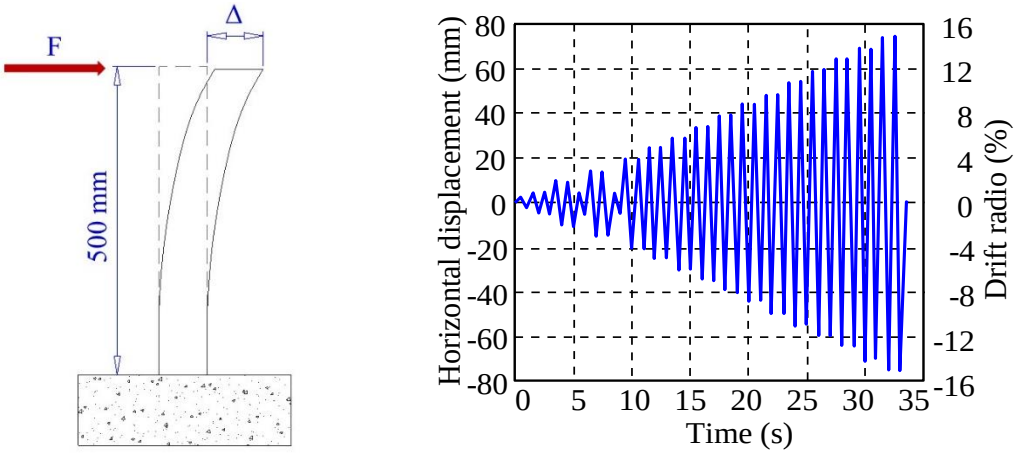

Fig. 4. Diagram of structure and load arrangement

Table 1 Parametric design of simulation materials.

Material		Compressive strength		Tensile strength		
		Ultimate	Creaking	Creaking	Peak	Ultimate
ECC	Strain (%)	-2.0	-0.5	0.01	3.8	6.0
	Stress (MPa)	0.0	-80.0	4.5	6.0	0.0
		Ultimate	Hardening	Elastic	Elastic	Hardening	Ultimate
Steel	Strain (%)	-16.0	-14.0	-0.2	0.2	14.0	16.0
	Stress (MPa)	-650.0	-620.0	-410.0	410.0	620.0	650.0

The numerical simulated relationships and the tested ones of the horizontal load versus the drift ratio of the cantilever column are shown in Fig. 5, respectively. From Fig. 5, it can be confirmed that the simulated results well agreed with the test ones. The maximum horizontal load (i.e., 18 kN) occurred when the drift ratio approached to 4.0%. The stress-strain relationship of the outermost layer of the ECC-reinforced column is shown in Fig. 6. The peak tensile stress response was up to 4.0 MPa corresponding to a tensile strain of 0.0001. The maximum tensile stress was 6.0 MPa when the tensile strain reached 0.038. The ultimate tensile strain was 0.056. The compressive stress was -80.0 MPa and the corresponding strain was -0.005. The ultimate compressive strain was -0.012. The results aforementioned show that the ECC material constitutive model (i.e., *ECC02*) implemented in OpenSees can be used to simulate the behavior of ECC-reinforced column properly.

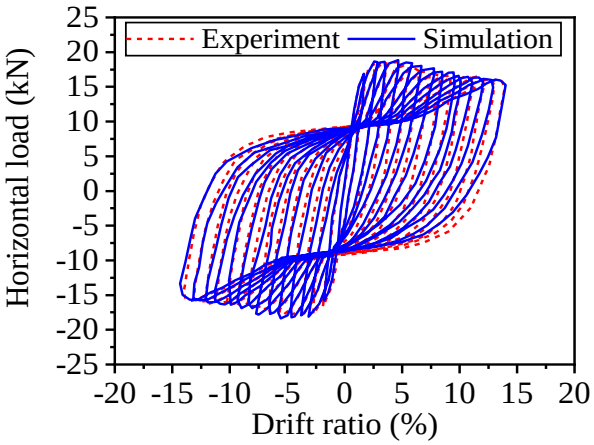

Fig. 5. Horizontal load vs. drift ratio

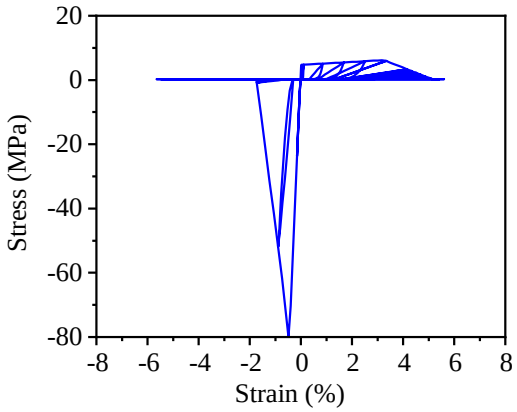

Fig. 6. The strain-stress response of ECC material

4.1.2 ECC-reinforced bridge pier under cyclic loading

A quasi-static test on a 1/5 scale ECC-RC bridge pier is used to investigate the applicability and accuracy of the proposed ECC constitutive model [38]. The bridge pier is 1.143 m high, measured from the top of the footing to the center of the bent cap, with a 0.254 m diameter section. The plastic hinge region (i.e., 0.5 m) of the pier was made up of the ECC material to avoid seismic damage and the rest part was composed of the normal concrete. A total of 8 longitudinal SMA bars were arranged uniformly in a circular pattern in the plastic hinge region of the pier and the rest part was reinforced by the reinforcing bar. The couplers were used to connect the SMA bars and the reinforcing ones. More detailed information about the material (i.e., ECC material, SMA bar, normal concrete and reinforcing bar) can be obtained from the reference [38]. The loading began with one complete cycle in the push-and-pull direction to 0.25% drift ratio. The subsequent drift ratios were 0.5, 1.0, 1.5, 2.0, 3.0, 4.0, 5.0, 7.0, 10.0, 12.0 and 14.0%. Two cycles were conducted at each drift ratio. The FE model of the pier was established in OpenSees. A total of five displacement-based Euler-Bernoulli fiber beam-column elements were used to model the pier shaft and two rigid elements were

employed to model the bent cap. The material nonlinearities of the normal concrete and the ECC material were considered using *Concrete02* and *ECC02* materials, respectively. The *Steel02* material was used to simulate the behavior of the reinforcement. The corotational transformation algorithm was used to consider the geometric nonlinearity of the pier. The experimental and numerical results of the shear force versus the displacement at loading point are shown in Fig. 7. It demonstrates that the numerical simulation results matched reasonably well with the test ones.

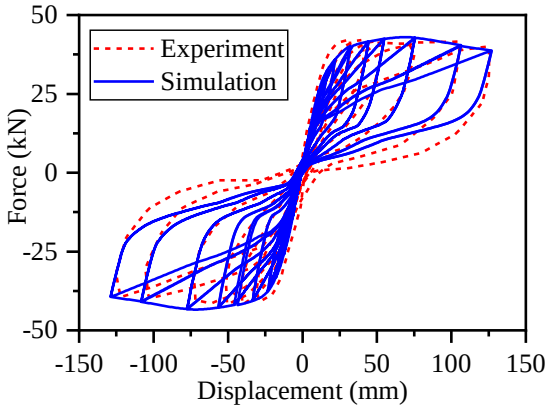

Fig. 7. Comparison of numerically simulated results and test ones

4.1.3 Dynamic performance of the ECC-reinforced frame under earthquake loading

To reconfirm the effectiveness and accuracy of the ECC constitutive model in modeling ECC-reinforced structures under earthquake loading, a 2-story 2-bay ECC-reinforced plane frame presented in the reference [39] is selected as a benchmark for demonstration. The diagram of the ECC-reinforced plane frame is shown in Fig. 8, where the detailed design information of the beam and the column are also presented. The diameters of the longitudinal reinforcing bar and the stirrup are 2.72 cm 0.98 cm, respectively. The nonlinear FE model of the plane frame was established in OpenSees. Each beam and column were modeled by five displacement-based Euler-Bernoulli fiber elements. The material nonlinearities of the ECC and the reinforcing bar were considered by the *ECC02* and *Steel02* materials, respectively. In addition to the material nonlinearity, the geometric nonlinearity of the frame was also considered using corotational transformation algorithm. The external earthquake excitation is presented in Fig. 9. The experimental and numerical results of lateral force and bending moment at the central point of the left column at ground floor are shown in Fig. 10. It indicates that the numerical results gave an accurate prediction of the actual behavior.

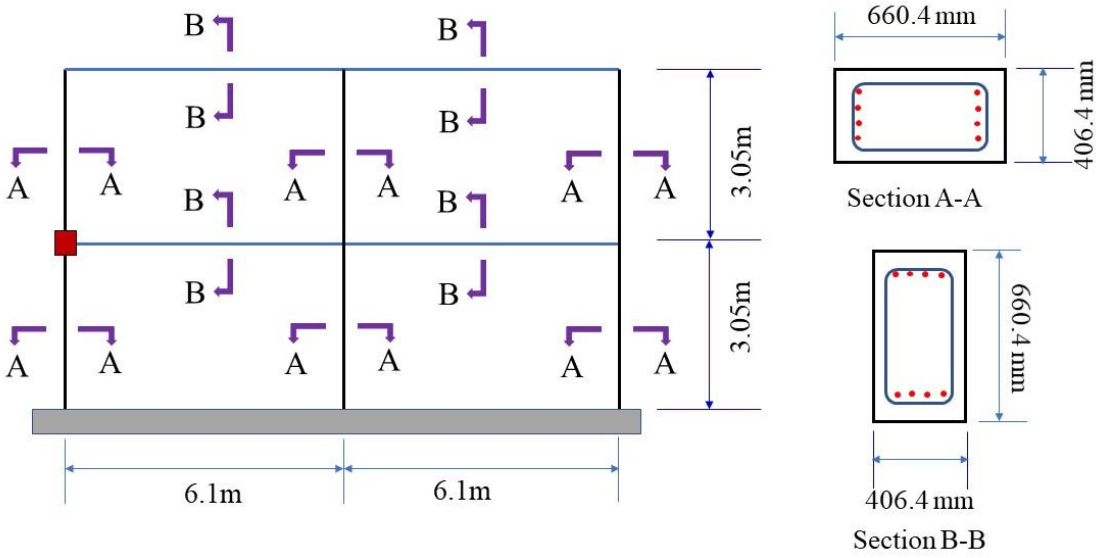

Fig. 8. 2-story 2-bay ECC-reinforced frame

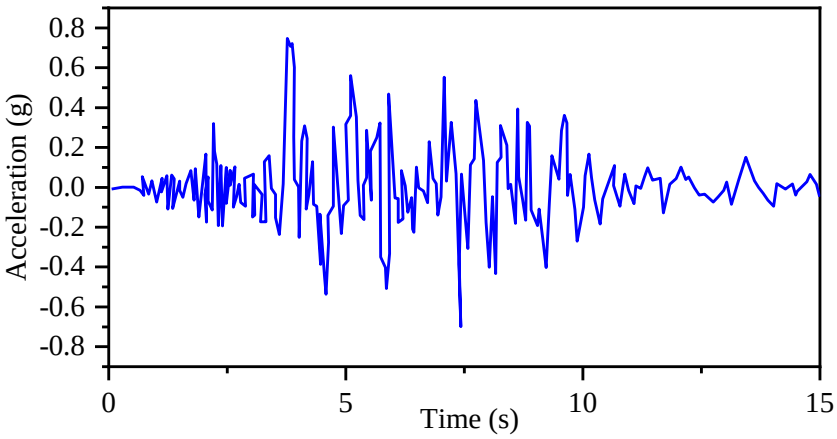

Fig. 9. The earthquake ground motion

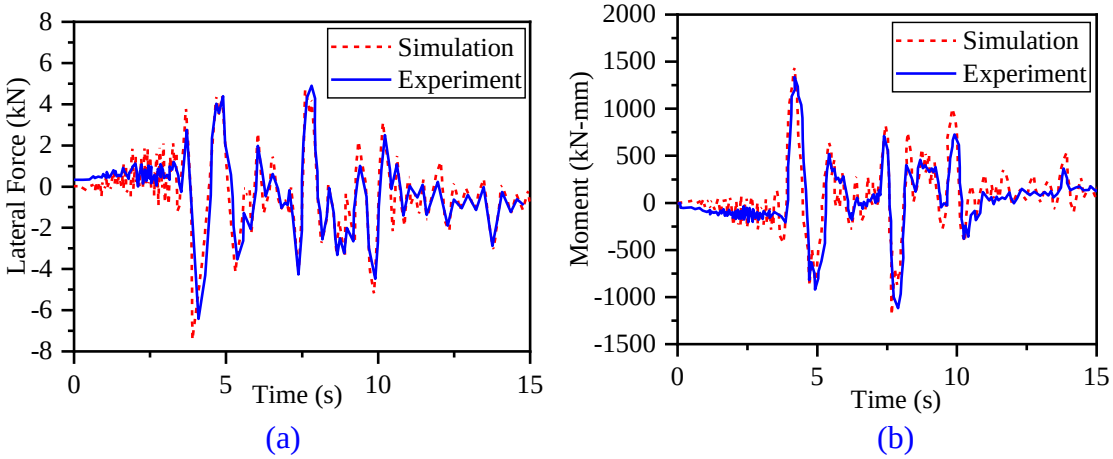

Fig. 10 Seismic response comparison between numerical simulation and test

(a) lateral force and (b) bending moment

5. Application example

The seismic analyses of an ECC-reinforced bridge and a similar RC bridge are firstly assessed and compared. Sensitivity analyses are subsequently conducted for the two bridges using both DDM-based and FDM-based methods. The efficiency and accuracy associated with these two sensitivity analysis methods are compared at last.

5.1. Seismic and sensitivity analysis of an ECC-reinforced bridge under earthquake loading

A prototype continuous bridge consists of two equal spans of 20 m. The configuration of the bridge and the detailed geometries of the twin-box girder, pier, and abutment are illustrated in Figs. 11 and 12. The height and the width of the RC twin-box girder are 1.2 m and 12.5 m, respectively. The only difference between two bridges is the material of the pier. One is reinforced ECC and another is reinforced normal concrete. The clear height and diameter of the column are 7.0 m and 0.9 m, respectively. Each column consists of 24 reinforcing bars with the diameter of 25 mm resulting in a longitudinal reinforcement ratio of 3.0%. The diameter of the stirrup is 16 mm and the spacing between two adjacent stirrups is 0.075 m resulting in a volumetric ratio of 0.6%. The properties of the reinforcing steel, concrete and the ECC material are shown in the Table 2. For the RC bridge, the concrete compressive strength of the pier is set as the same as that of the ECC material (e.g., 80 MPa) for reasonable comparison purpose. The compressive cracking and ultimate strain of the ECC material are 2.5 times of that of concrete, so the Young's modulus of the ECC material is lower than that of the normal concrete when the compressive strength is same. In the tensile state, the normal concrete is a brittle material and its ultimate tensile strain is very small (i.e., 0.12%). Because the ECC material has good ductility, its ultimate tensile strain can reach 6%. The maximum stress of the reinforcing steel in elastic state is 280 MPa, and it reaches 320 MPa after hardening. The strength of the ECC material and the normal concrete materials in this case can be obtained from the reference [5].

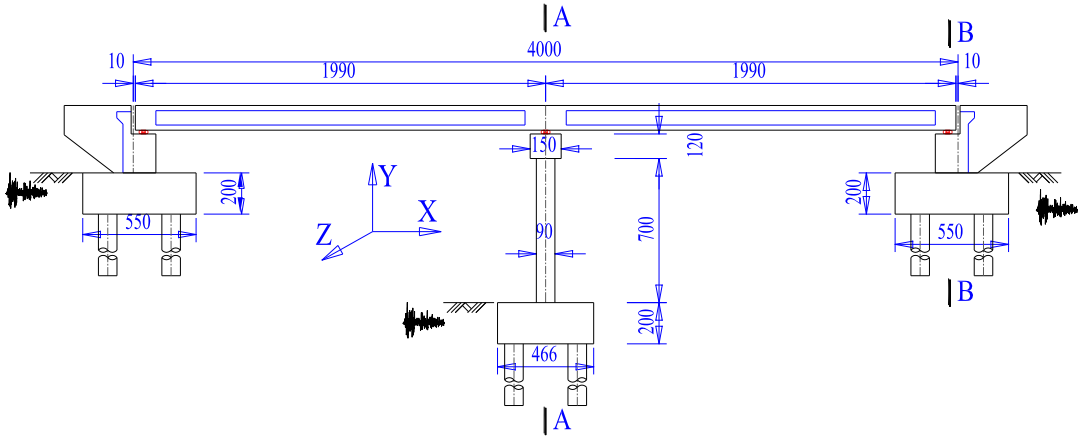

Fig. 11. Configuration of a bridge with ECC material reinforced/RC pier (unit: cm)

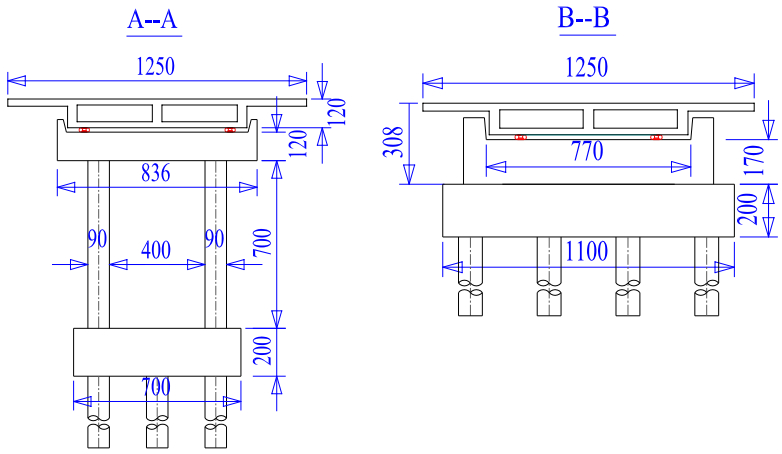

Fig. 12. The section views of the pier and abutment (unit: cm)

Table 2 Properties of the materials

material		Compressive strength			Tensile strength		
		creaking	peak	ultimate	creaking	peak	ultimate
ECC	Strain (%)	-0.5	-0.5	-2.0	0.01	3.8	6
	Stress (MPa)	-80	-80	0.0	6.0	8.0	0.0
Normal concrete	Strain (%)	-0.2	-0.2	-0.5	0.003	0.003	0.12
	Stress (MPa)	-80	-80	0.0	4.5	4.5	0
		elastic	hardening	ultimate	elastic	hardening	ultimate
Reinforcement	Strain (%)	-0.2	-14	-16	0.2	14	16
	Stress (MPa)	-280	-320	-320	280	320	320

A 3D bridge model with ECC-reinforced pier and a bridge model with RC pier are established in OpenSees, respectively. The detailed model of the bridge with the ECC-reinforced pier is shown in Fig. 13. Each span of the main girder is divided into 14 elastic beam-column elements. Each ECC-reinforced pier is divided into 10 nonlinear beam-column elements with fiber section, in which the concrete and reinforcing steel are simulated using uniaxial material models of the ECC material and Giuffré-Menegotto-Pinto Model with Isotropic Strain Hardening (named *Steel02* in OpenSees), respectively. Their stress-strain relationship and envelope will be described in the subsequent paragraph. The same element mesh scheme is applied to the RC pier except the material model *ECC02* is replaced by the Linear Tension Softening model of concrete (named *Concrete02* in OpenSees). Apart from the

nonlinear material properties of the normal concrete, the ECC material and reinforcement, the geometric nonlinearity of the bridge is also incorporated using the co-rotational geometric transformation algorithm [36]. The RC abutments is modeled by elastic beam-column element. Two conventional sliding friction bearings are placed on each abutment and two fixed bearings are mounted on each bent cap. The behavior of the sliding friction bearing is modeled by an ideally elastic-plastic model, of which the yielding strength is the product of the friction coefficient and the normal force.

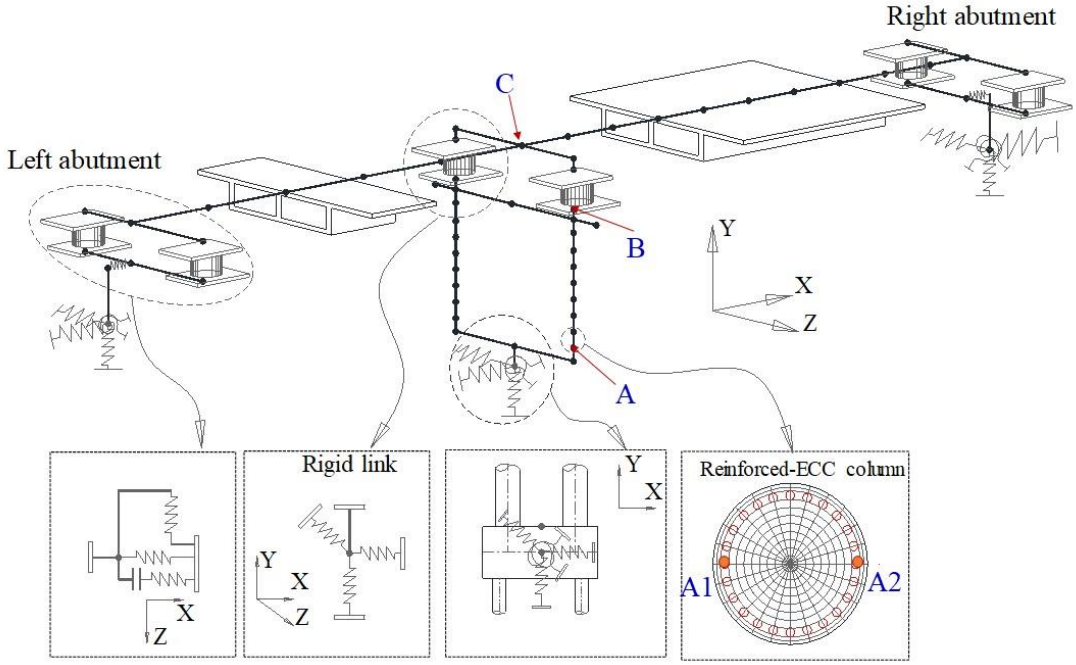

Fig. 13. FE model of the bridge with ECC material reinforced/RC pier

After a static analysis of the bridge under gravity, a uniform base excitation along the X direction is applied to the bridge. The Sep. 2nd, 1971 San Fernando seismic record No. 9 is selected as the earthquake loading (see Fig. 14). The displacement responses in the X direction at the points B and C of the ECC-reinforced and the RC bridges are presented in Fig. 15 for comparison. From Fig. 15, it can be observed that during the period from 0 to 4.0 seconds when the earthquake load is relatively small, the two bridges stay in elastic stage, and the displacement of the ECC-reinforced bridge is similar to that of the RC bridge. The maximum displacement of the ECC-reinforced bridge occurs at 4.5 seconds with the amplitude of 0.48 m which is 15% less than that of the RC bridge. After 4.5 s, the ECC-reinforced bridge recovered to its original position due to the superior resilience of the ECC material. The RC bridge experienced permanent residual deformation (around 0.34 m and 0.35 m at the points B and C, respectively).

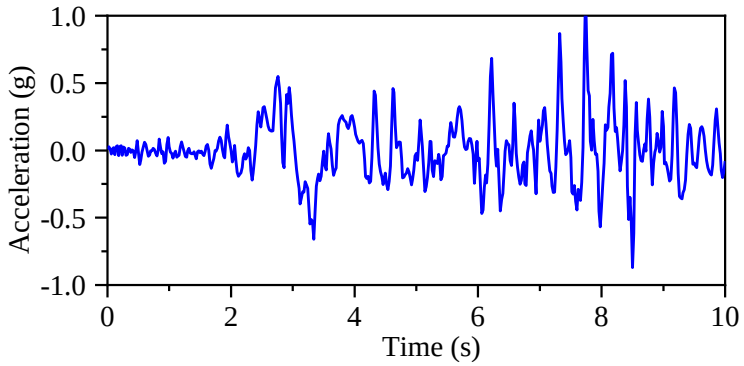

Fig. 14. San Fernando earthquake ground motion

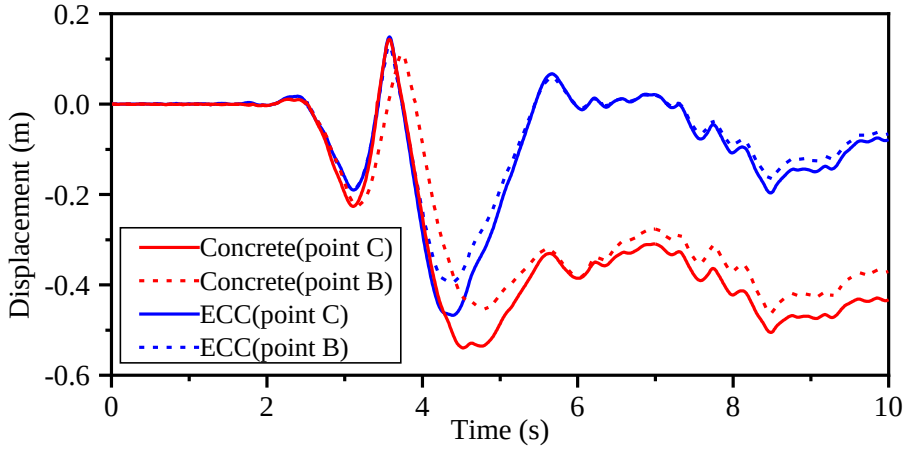

Fig. 15. Displacement responses at points B and C of ECC-reinforced and RC bridges

In order to further investigate the effect of replacing the normal concrete by the ECC material on the seismic response, the stress-strain responses of the ECC material reinforced and the RC columns are compared. Fig. 16 shows the stress-strain responses of two representative fibers in section A located at bottom of the plastic hinge region of the pier (see Fig. 13). The bridge yielded significantly (see Figs. 16a and b) when the normal concrete fiber lost tensile capacity, while the ECC fiber can still sustain tensile force due to its higher tensile resistant capacity. The normal concrete fiber sustains larger tensile strain (i.e., 13% larger) than that of the ECC fiber for smaller tensile capacity. The compressive strain of the ECC fiber is slightly larger than that of the normal concrete due to the lower Young's modulus. Figs. 16c and 16d show the comparative stress-strain responses of the steel fibers at the same section of the column. The tensile strains of the steel fibers in the ECC-reinforced pier are smaller (23% less) than those of the RC pier resulting from higher tensile capacity. However, the compressive strains of the steel fibers in the ECC-reinforced pier are larger than those in the RC pier (12% larger) due to lower Young's modulus. Overall, the seismic performance of ECC-reinforced bridge is better than the conventional RC bridge.

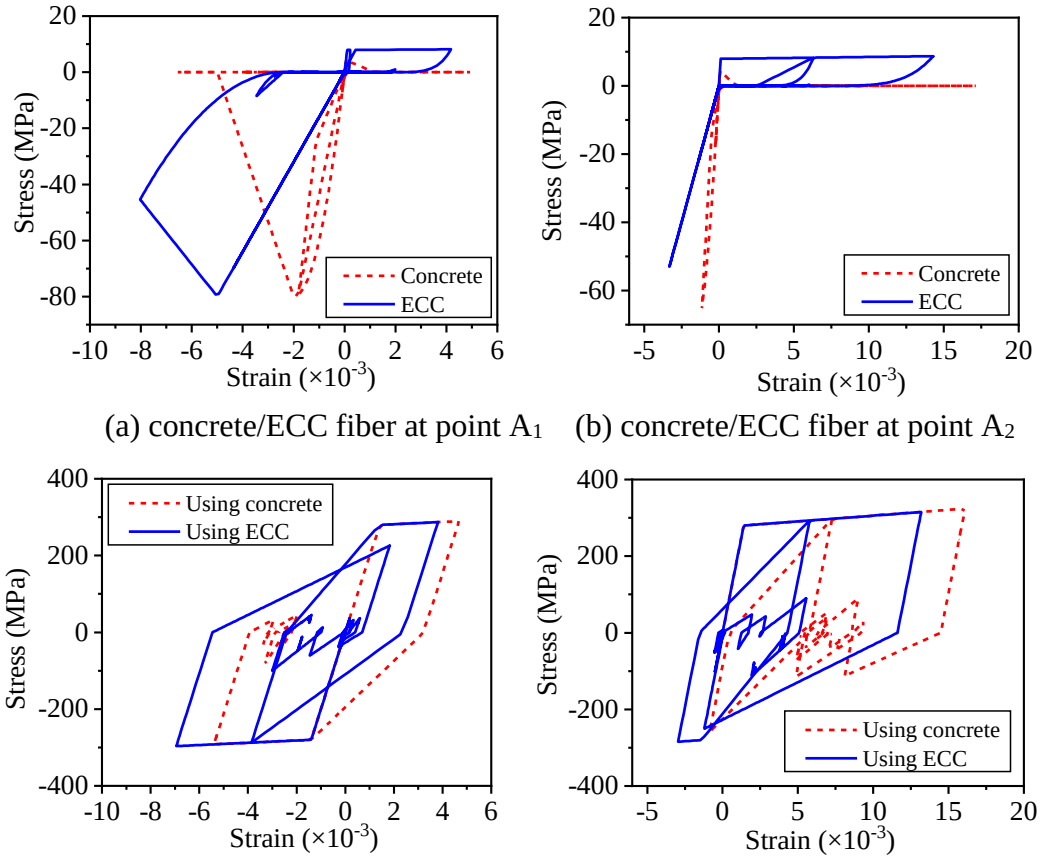

(a) concrete/ECC fiber at point A_1 (b) concrete/ECC fiber at point A_2

(c) steel fiber at point A_1 (d) steel fiber at point A_2

Fig. 16. Stress-strain responses of cover concrete at point A

After assessing the performance of the ECC-reinforced bridge and the RC bridge, sensitivity analysis is necessary to aid the design and optimization of such structures. The sensitivity analyses are conducted using both the developed DDM- and the FDM-based approaches. FDM replaces every derivative with the approximate formula of finite difference, and then transforms the problem of solving partial differential equation into the problem of solving algebraic equation. The FDM-based sensitivities are obtained by,

$$\left.\frac{\partial \mathbf{R}(t,\theta)}{\partial \theta}\right|_{\theta=\theta_0} \approx \frac{\mathbf{R}(t,\theta_0+\Delta\theta)-\mathbf{R}(t,\theta_0)}{\Delta\theta} \tag{12}$$

where response sensitives $\left.\frac{\partial \mathbf{R}(t,\theta)}{\partial \theta}\right|_{\theta=\theta_0}$ can be calculated by the difference between $\mathbf{R}(t,\theta_0+\Delta\theta)$ and $\mathbf{R}(t,\theta_0)$. $\mathbf{R}(t,\theta_0+\Delta\theta)$ represents the structural response after adding a disturbance value $\Delta\theta$ based on the parameters which is cared during the sensitivity analysis. When the disturbance value $\Delta\theta$ decreases, the FDM results are more and more close to the analytical solution of sensitivities at θ_0. However, due to the truncation error, when the

disturbance value is too small, the FDM results will diverge. This is the reason why FDM results are not as accurate as DDM results. Fig. 17 shows the comparative sensitivity results of displacement in the X direction at point B (see Fig. 13) with respect to the cracking tensile stress σ_{t0}. From Fig. 17, it can be observed that the results of FDM converges asymptotically to the DDM-based results when the size of perturbation reducing from 1×10^{-2} to 1×10^{-8}. However, when the perturbation size is too smaller (e.g., less than 1×10^{-10}), the FDM-based results diverges due to the increasing round-off error.

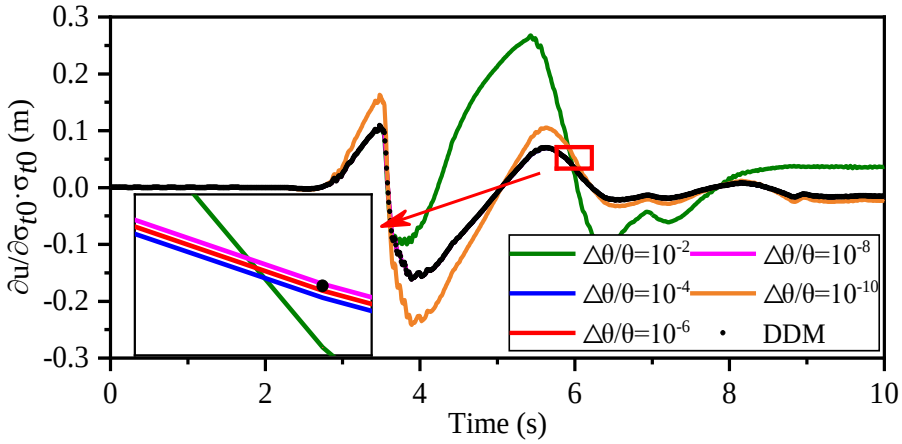

Fig. 17. Sensitivities of displacement at point B to σ_{t0} using DDM vs. FDM with different perturbation sizes

Fig.14 shows the comparison results of the displacement sensitivity at point B in the X direction to the peak tensile stress σ_{tp} obtained from the DDM- and FDM-based algorithms. It indicates that the FDM-based result converges to the DDM-based ones until the reducing perturbation size reaches 1.0×10^{-7}. The optimum perturbation size is not easy to determine for the FDM-based algorithm without a careful convergence investigation. When the disturbance value is too large or too small, the result of FDM will deviate from the analytical solution. Consequently, the DDM-based algorithm is associated with stronger robustness and performs better than the FDM-base one in terms of accuracy and efficiency. Apparently, DDM could efficiently aid the analysis of relative importance of material parameters and capture the complex behavior of structural systems especially approaching their failure state.

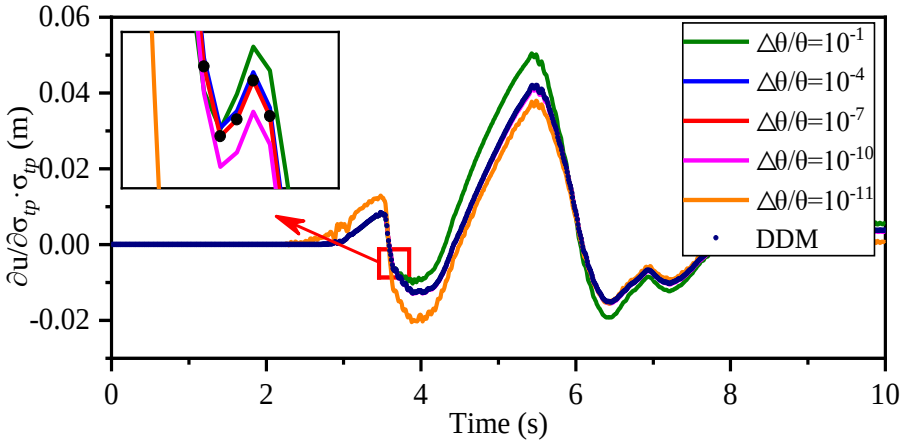

Fig. 18. Sensitivities of displacement at point B to σ_{tp} using DDM vs. FDM with different perturbation sizes

As one of the most crucial applications of the DDM-based sensitivity analysis, the relative sensitivity of the ECC parameters to the seismic responses of the bridge can be quantified in terms of the maximum absolute value of the normalized response sensitivity time history, i.e., $\frac{\partial u}{\partial \theta}\theta$. Fig. 19 shows the normalized sensitivities of the displacement at point B in the X direction to the five most sensitive ECC parameters. The rank of relative sensitivity and importance of the ECC parameters (in a descending order) is: the cracking tensile stress σ_{t0}, the cracking compressive strain ε_{c0}, the cracking compressive stress σ_{c0}, the peak compressive strain ε_{cp}, and the peak tensile stress σ_{tp}. From these observations, it is clear that the cracking tensile stress σ_{t0} is the controlling parameter significantly affecting the seismic displacement response. In practice, the parameter σ_{t0} of the ECC material is relatively easy to enhance by modifying the mix ratio resulting in a more resilient bridge. The displacement response sensitivity to the elastic parameters (e.g., σ_{t0}, ε_{c0} and σ_{c0}) increases rapidly when the bridge system stay in linear range (i.e. during the time period [2.5, 4.0]). However, the sensitivity to the elastic parameters significantly reduces and the sensitivity ranks of the plastic parameters remarkably rises after 4.5 seconds, because the seismic behavior of the pier changes from the elastic state to the plastic one. Consequently, the sensitivity and importance of each parameter can be ranked in terms of the elastic and the plastic states, respectively. The response sensitivity analysis results can provide useful information for efficiently improving the seismic resistance capacity of the bridge structure.

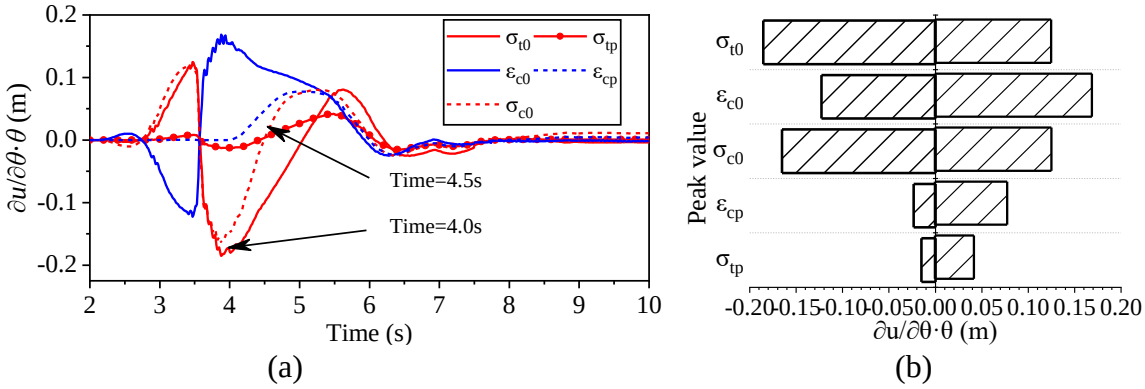

Fig. 19 Relative importance of ECC parameters regarding the horizontal displacement of point B (a) the response sensitivities of the five most important parameters (b) tornado diagram of sensitivity analysis

To compare the influences of the same parameter of the ECC material and the normal concrete on the displacement responses along X direction at points B and C of the ECC-reinforced and the RC bridges, the displacement sensitivities to the peak compressive stress σ_{cp} are shown in Fig. 20. The sensitivities to σ_{cp} of the normal concrete are consistently larger than those of the ECC, and the evident difference appears in the period from 6.0 to 10.0 seconds. This is because the ECC material only undergoes a little damage after 6.0 seconds and hence the response is not sensitive to the plastic parameters, while the response of normal concrete remains sensitive to the plastic parameters due to its significantly plastic deformation in the compressive region.

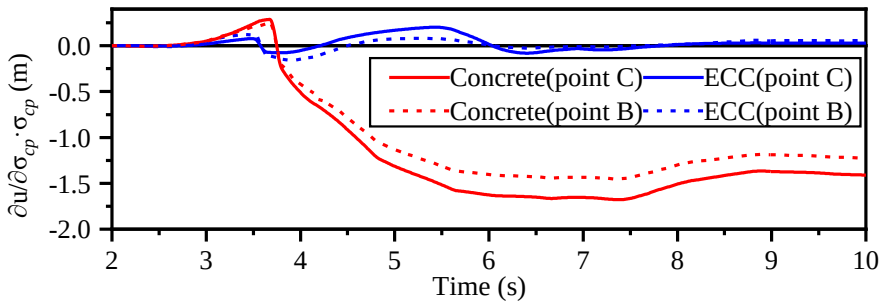

Fig. 20. Displacement sensitivities of ECC/concrete regarding σ_{cp} at points B and C

Similarly, the displacement response sensitivities at the points B and C of the ECC-reinforced and the RC bridges to the peak tensile stress σ_{tp} are plotted in Fig. 21, respectively. The displacement sensitivities of the ECC are similar to those of the normal concrete before 4.5 seconds when the two bridges both exhibits elastic performance. The σ_{tp} of the normal concrete becomes more sensitive than the ECC after 4.5 seconds, because the ECC material

slightly experiences plastic deformation in the tensile region while the normal concrete undergoes a large permanent tensile deformation.

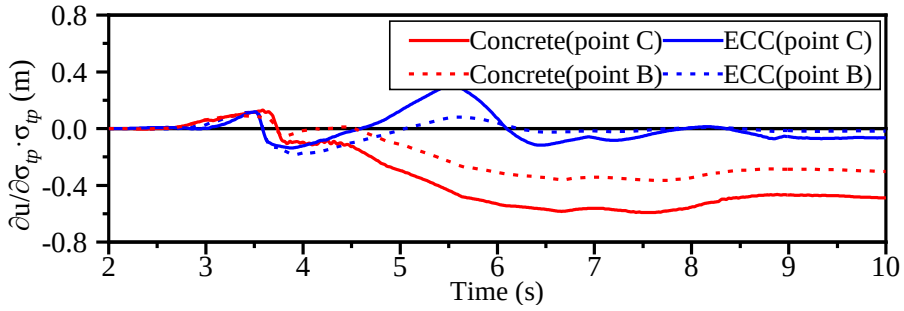

Fig. 21. Displacement sensitivities of ECC/concrete regarding σ_{tp} at points B and C

To compare the displacement response sensitivities to the reinforcement in the ECC-reinforced and the RC columns, the sensitivities of the displacement response at point B in X direction are shown in Fig. 22. It can be confirmed that the displacement response sensitivities of the RC column are consistently more sensitive to the reinforcement parameters than those of the ECC-reinforced column, as the reinforcement in the RC column sustains more tensile force than that of the reinforcement in the ECC-reinforced column.

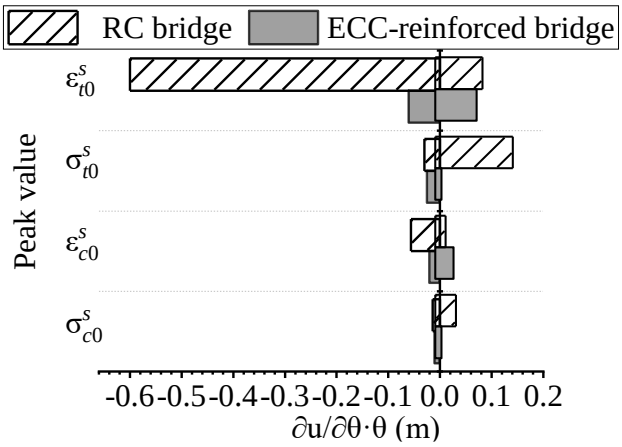

Fig. 22. Displacement sensitivities regarding the reinforcing steel parameters

The displacement sensitivities of RC bridge with respect to the yield tensile strain ε_{t0} and corresponding stress σ_{t0} are 6 times and 3 times of the ECC-reinforced bridge, respectively. As a result, the two most sensitive parameters controlling the displacement response are both tension-related parameters, i.e., the yield tensile strain ε_{t0} and corresponding stress σ_{t0} of the reinforcement. The compressive strengths of the normal concrete and the ECC are equal so that the compressive forces sustained by the reinforcement in the RC and the ECC-reinforced column are at similar level. Thus, it is easy to explain why the displacement response sensitivities to such compression-related parameters as the yield

compressive strain ε_{c0} and corresponding stress σ_{c0} of the reinforcement are remarkably smaller than those tension-related parameters.

Sensitivity analysis is applicable to different seismic load conditions. For the same structure, the sensitivity analysis results are different under different seismic loads. Sensitivity analysis provides a tool for further analysis of structural responses. The Kumamoto-shi seismic wave recorded on April 14th, 2016 is used as loads for the continuous beam described above. The seismic wave is shown in Fig. 23. For the lateral displacement of the top of the pier, the sensitivity results of the most sensitive parameters are shown in Fig. 24, which are ranked in a descending order, including cracking strain ε_{t0}, peak tensile strain ε_{tp}, compressive hysteresis parameter α_c, cracking stress σ_{t0}, tensile hysteresis parameter α_t. Sensitivity analysis of both San Fernando and Kumamoto-shi earthquakes show that, the importance rank of parameters is very different for different seismic loads. The sensitivities of the ECC parameters are slightly higher than that under San Fernando seismic wave. Different from the previous conclusion, the most sensitive parameters under Kumamoto-Shi seismic wave are strain-related and hysteresis-related parameters (while the most sensitive parameters are stress-related parameters under San Fernando seismic wave). It illustrates that the good ductility and hysteretic capacity of the ECC materials play a greater role to control the deformation of the structure. At the same time, it also shows that the ECC components have higher nonlinear degree under Kumamoto-Shi seismic wave, and their hysteretic capacity is more important to limit the structural deformation.

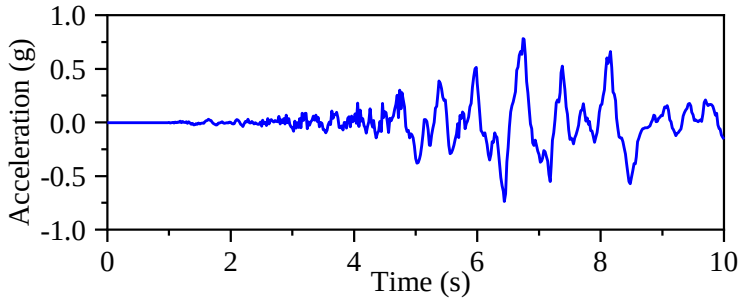

Fig. 23. The acceleration of Kumamoto-shi seismic waves

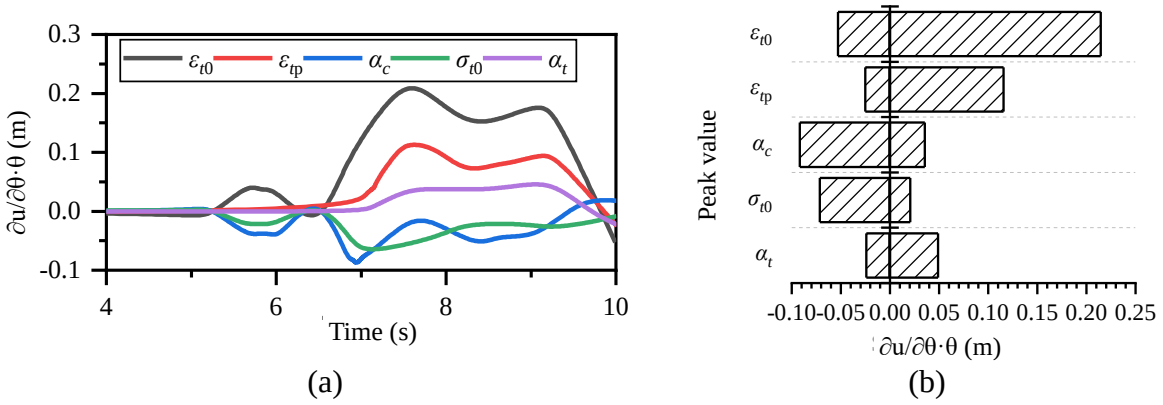

Fig. 24. Response sensitivities (a) response sensitivities of the five most important parameters and (b) tornado diagram of sensitivity analysis

5.2. Discussion on the relationships between structural dynamic response and sensitivity analysis result

Sensitivity analysis is a powerful tool in the fields such as gradient-based structural optimization, system identification, and FE model updating but does not directly affect the nonlinear analysis response of structure. A specific application of the sensitivity analysis is that it can be used to quantify which property of the material sensitive to the concerned dynamic responses for achieving a best cost-efficient structure design.

Taking the prototype ECC-reinforced bridge under seismic loads as an example, the sensitivity curves of each parameter indicate their use ratio in the ECC-reinforced components or structures. As shown in Fig. 19, the fluctuation of the ultimate tensile stress σ_{tp} was gentle and the value was relatively small, which implies that the ECC material had not reached the ultimate state, and the ultimate tensile stress had little influence on the ECC-reinforced components or structures. It means that we can appropriately reduce the cross-section area of the ECC-reinforced components aiming to reduce the construction cost. The sensitivity curves of the cracking compressive strain ε_{c0} changed sharply and the value was relatively large, which indicates that the ECC material can remarkably reduce the structural deformation under seismic excitation.

In conclusion, sensitivity analysis provides an efficient approach to find the most sensitive one among the properties of the investigated material for reducing the structural dynamic response and construction cost.

6. Conclusions

This paper reviews a uniaxial constitutive model of the promising ECC material and proposes a DDM-based sensitivity analysis algorithm. Then, the sensitivity analysis is integrated into OpenSees for establishing a sensitivity analysis framework. Two similar FE models of a prototype bridge are established in OpenSees except the different materials used in columns. The seismic performance of the ECC-reinforced bridge is assessed and compared with the RC bridge. A series of sensitivity analysis studies are following conducted. Several conclusions can be drawn from these studies.

1. The results from seismic performance assessment indicate that the ECC material-reinforced bridge can almost recover to its original position after earthquakes due to the resilient property of the ECC material, while the RC bridge always undergoes large permanent residual deformation.

2. The response sensitivity analysis results show that the FDM-based algorithm can asymptotically convergent to the DDM-based one with reducing perturbation size, which means both the accuracy and efficiency of the DDM-based algorithm are superior than those of the FDM-based one.

3. The displacement response sensitivities to the elastic or plastic parameters of the normal concrete and the ECC material are time-dependent during earthquakes.

4. The displacements of the RC bridge are consistently more sensitive to the plastic parameters of the reinforcement, especially for the tensile strength, than those of the ECC-reinforced bridge, as the tensile capacity of the normal concrete is smaller than that of the ECC material.

5. This paper provides an efficient and accurate sensitivity analysis framework for the ECC-reinforced structures subjected to seismic loads.

Acknowledgements

The financial supported by the National Key Research and Development Program of China with Grant No. 2016YFC0701106 and China's National Natural Science Foundation with Grant Nos. 51978591, 51978513 and 51578473 are greatly acknowledged. Any opinions and concluding remarks presented in this paper are entirely those of the authors.

References

[1] Kesner KE, Sarah LB. Experimental response of precast infill panel connections and panels made with DFRCC. J Adv Concr Technol 2003;1(3):327-333.

[2] Parra-Montesinos G, Wight JK. Seismic response of exterior RC column-to-steel beam connections. J Struct Eng 2000;126(10):1113-1121.

[3] Fischer G, Li VC. Effect of matrix ductility on deformation behavior of steel-reinforced ECC flexural members under reversed cyclic loading conditions. ACI Struct J 2002;99(6):781-790.

[4] Li VC, Wang S. Flexural behaviors of glass fiber-reinforced polymer (GFRP) reinforced engineered cementitious composite beams. Mater J 2002;99(1):11-21.

[5] Li VC. Engineered Cementitious Composites (ECC) - Material, Structural, and Durability Performance, Concrete Construction Engineering Handbook, 2008.

[6] Li VC, Leung CK. Steady state and multiple cracking of short random fiber composites. J Eng Mech 1992;188(11):2246, 264

[7] Li VC, Stang H, Krenchel H. Micromechanics of crack bridging in fiber reinforced concrete. Mater Struct 1993;26(8):486-494.

[8] Li VC. On Engineered Cementitious Composites (ECC) - A Review of the Material and its Applications. J Adv Concr Technol 2003;1(2):215-230.

[9] Dhawale AW, Joshi VP. Engineered cementitious composites for structural applications. J Mater Civ Eng 1998;10(2):66-69.

[10] Fischer G, Li VC. Deformation behavior of fiber-reinforced polymer reinforced Engineered Cementitious Composite (ECC) flexural members under reversed cyclic loading conditions, ACI Struct J 2003;100(1):25-35

[11] Pan Z. Study on mechanical properties of cost-effective polyvinyl alcohol engineered cementitious composites (PVA-ECC). Constr Build Mater 2015; 78:397-404.

[12] Kim YY. Mechanical performance of sprayed engineered cementitious composite using wet-mix shotcreting process for repair applications. Mater J 2004;101(1):42-49.

[13] Zheng Y, Dong Y, Li Y. Resilience and life-cycle performance of smart bridges with shape memory alloy (SMA)-cable-based bearings. Constr Build Mater 2018; 158: 389-400.

[14] Zheng Y, Xu YL, Zhan S. Seismic responses and collapse of a RC pedestrian cable-stayed bridge: shake table tests. Int J Struct Stab Dyn 2019;19(7):1950067.

[15] Simo JC, Ju JW. Strain- and stress-based continuum damage models—I. Formulation. Int J Sol Struct 1987;23(7): 821-840.

[17] De Borst R, Nauta P. Non-orthogonal cracks in a smeared finite element model. Eng Comp 1985;2(3):35-46.

[18] Han TS, Peter HF, Sarah LB. Simulation of highly ductile fiber-reinforced cement-based composite components under cyclic loading. Struct J 2003;100(6):749-757.

[19] Parra-Montesinos GJ. High-performance fiber-reinforced cement composites: an alternative for seismic design of structures. ACI Struct J 2005;102(5): 668.

[20] Kesner KE, Billington SL, Douglas KS. Cyclic response of highly ductile fiber-reinforced cement-based composites. Mater J 2003;100(5):381-390.

[21] Conte JP, Vijalapura PK, Meghella M. Consistent finite-element response sensitivity analysis. J Eng Mech 2003;129(12):1380-1393.

[22] Barbato M, Gu Q, Conte JP. Probabilistic push-over analysis of structural and soil-structure systems. J Struct Eng 2010;136(11):1330-1341.

[23] Ditlevsen O, Henrik OM. Structural reliability methods. Vol. 178. New York: Wiley, 1996.

[24] Zhang Y, Armen DK. Dynamic response sensitivity of inelastic structures. Comp Methods Appl Mech Eng 1993;108(1-2):23-36.

[25] Scott MH, Franchin P, Fenves GL, Filippou FC. Response sensitivity for nonlinear beam–column elements. J Struct Eng 2004;130(9):1281-1288.

[26] Haukaas T, Kiureghian AD. Strategies for finding the design point in non-linear finite element reliability analysis. Prob Eng Mech 2006;21(2):133-147.

[27] Conte JP. Finite element response sensitivity analysis in earthquake engineering. Earthquake engineering frontiers in the new millennium 2001:395-401.

[28] Conte JP, Barbato M, Spacone E. Finite element response sensitivity analysis using force-based frame models. Int J Numer Methods Eng 2004;59(13):1781-1820.

[29] Gu Q, Barbato M, Conte JP. Handling of constraints in finite-element response sensitivity analysis. J Eng Mech 2009;135(12):1427-1438.

[30] Gu Q, Conte JP, Elgamal A, Yang Z. Finite element response sensitivity analysis of multi-yield-surface J2 plasticity model by direct differentiation method. Comp Methods Appl Mech Eng 2009;198(30-32):2272-2285.

[31] Barbato M, Gu Q, Conte JP. Response sensitivity and probabilistic response analyses of reinforced concrete frame structures. Proceedings of the 8th NCEE,2006:18-22.

[32] Zona A, Barbato M, Conte JP. Finite element response sensitivity analysis of continuous steel-concrete composite girders. Steel and Composite Structures 6, no. 3,2006:183.

[33] Habibi A, Moharrami H. Nonlinear sensitivity analysis of reinforced concrete frames. Finite Elements in Analysis and Design 46, no. 7,2010: 571-584.

[34] Mazzoni S, McKenna F, Scott MH and Fenves GL. OpenSees command language manual. Pacific Earthquake Engineering Research (PEER) Center, 2006.

[35] Billington, S.L., and Kesner, K.E. Development of Ductile Cement-based Composites for Seismic Strengthening and Retrofit. Proceedings for the 2nd International Conference on Engineering Materials. San Jose, CA, August, 2001.

[36] Zheng Y, Dong Y. Performance-based assessment of bridges with steel-SMA reinforced piers in a life-cycle context by numerical approach. Bull Earthq Eng 2019;17(3);1667-1688.

[37] Crisfield MA. A consistent co-rotational formulation for non-linear, three-dimensional, beam-elements. Comp Methods Appl Mech Eng 1990;81(2):131-150.

[38] Saiidi MS, O'Brien M, Sadrossadat-Zadeh M. Cyclic response of concrete bridge columns using superelastic nitinol and bendable concrete. ACI Struct J 2009;106(1):69-77.

[39] Gencturk B Multi-objective optimal seismic design of building using advanced engineering materials. PhD thesis, Department of Civil and Environmental Engineering, University of Illinois at Urbana-Champaign, Urbana, 2011.